Nanotechnology **21** (2010) 065306 (6pp) doi:10.1088/0957-4484/21/6/065306

Functional plasmonic antenna scanning probes fabricated by induced-deposition mask lithography

A Weber-Bargioni[1,3], A Schwartzberg[1], M Schmidt[2], B Harteneck[1], D F Ogletree[1], P J Schuck[1,3] and S Cabrini[1,3]

[1] Molecular Foundry, Lawrence Berkeley National Laboratory, 1 Cyclotron Road, Berkeley, CA 94720, USA
[2] Energy Biosciences Institute, Calvin Laboratory, University of California at Berkeley, Berkeley, CA 94720, USA

E-mail: afweber-bargioni@lbl.gov, amschwartzberg@lbl.gov, mwbschmidt@lbl.gov, bdharteneck@lbl.gov, dfogletree@lbl.gov, pjschuck@lbl.gov and scabrini@lbl.gov

Received 19 August 2009, in final form 13 November 2009
Published 11 January 2010
Online at stacks.iop.org/Nano/21/065306

Abstract
We have fabricated plasmonic bowtie antennae on the apex of silicon atomic-force microscope cantilever tips that enhance the local silicon Raman scattering intensity by $\sim 4 \times 10^4$ when excited near the antenna resonance. The antennae were fabricated using a novel method, induced-deposition mask lithography (IDML), capable of creating high-purity metallic nanostructures on non-planar, non-conducting substrates with high repeatability. IDML involves electron-beam-induced deposition of a W or SiO_x hard mask on the material to be pattered, here a 20 nm Au film, followed by Ar ion etching to remove the mask and the unmasked gold, leaving a chemically pure Au bowtie antenna. Antenna function and reproducibility was confirmed by comparing Raman spectra for excitation polarized parallel and perpendicular to the antenna axis, as well as by dark-field spectroscopic characterization of resonant modes. The field enhancement of these plasmonic AFM antennae tips was comparable with antennae produced by electron-beam lithography on flat substrates.

S Supplementary data are available from stacks.iop.org/Nano/21/065306/mmedia

1. Introduction

Nanophotonics and nanoplasmonics are emerging fields that attempt to direct and control light at the nanometer scale, well beyond the diffraction limit [1–7]. Tip-enhanced Raman spectroscopy (TERS) [8] is a significant application of near-field optics, which has been used to image single proteins [9] and carbon nanotubes [10, 11] and is potentially capable of chemical mapping with molecular resolution [12]. Optical antennae create ultra-enhanced, extremely localized optical fields by efficiently coupling photons to surface plasmons in metal nanoparticles. Antennas are tuned structures where the specific resonances depend sensitively on the shape, cavity size, dielectric functions of the antenna material and the surrounding media [13–15], and, for coupled-particle plasmonic antennae, the gap size [16]. Of particular interest are bowtie-like antennae geometries [17], which can produce highly localized and strongly enhanced optical near fields [7].

The application of plasmonic devices in spectroscopy has been limited by the lack of methods for integrating specifically engineered plasmonic nanostructures into actual devices; for example, fabricating plasmonic antennae on pre-existing AFM cantilevers for next-generation near-field optical probes. This work reports a significant advance in nanoplasmonic structure fabrication, namely the development of the novel technique of induced-deposition mask lithography (IDML), capable of creating high-purity metallic nanostructures on non-planar, non-conducting substrates with good reproducibility.

To date, optical antennae have been fabricated by a number of different methods, each with its own drawbacks. High-resolution devices have been fabricated with state-of-the-art electron-beam lithography (EBL) [18]. EBL combined

[3] Authors to whom any correspondence should be addressed.

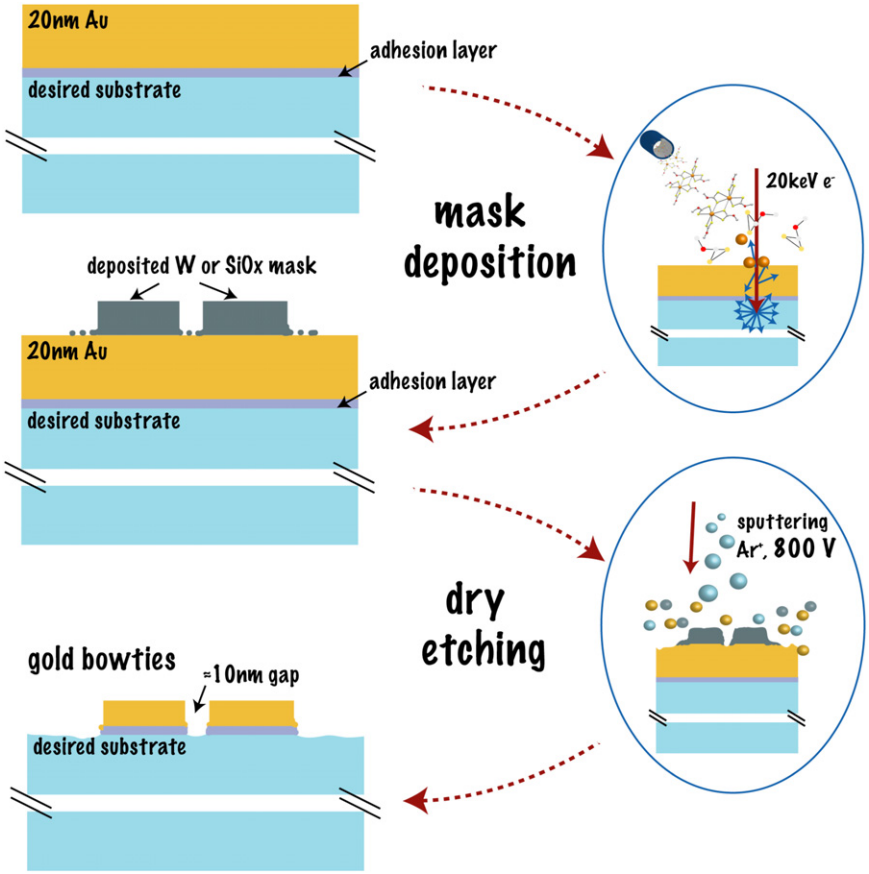

Figure 1. IDML nanofabrication process. First the antenna material is evaporated onto the substrate of interest. Electron-beam-induced deposition is used to define a precisely positioned etch mask. Subsequent Ar^+ milling transfers the mask shape into the underlying material.

with conventional lithography is well suited to wafer-scale batch fabrication of integrated plasmonic devices on flat conductive substrates using spin-on resists, but is difficult to apply in complex geometries such as cantilever sensors. Well-defined metal nanostructures can be created by chemical synthesis [19] but the specific placement and attachment to functional devices is challenging [20]. Shadow evaporation techniques [16] are restricted to flat surfaces, and the variety of possible shapes is limited. Focused-ion-beam (FIB) milling is very flexible [21], but the Ga contamination of the resulting structure can short-out antennae or modify the plasmonic response of metal structures due to the strongly confined nature of the fields [22]. This is because small isolated nanostructures with zeptoliter mode volumes are extremely sensitive to contamination [23]. Finally, focused-electron-beam-induced deposition (FEBID) [24] can directly write high-resolution structures (<5 nm [25]) with precise placement, independent of the local topography, but the variety of materials that can be deposited is limited and they are often severely contaminated with C and O. FEBID deposition of Au has been demonstrated [26], but neither the precursor molecules nor deposition systems are commercially available.

In contrast, IDML allows the precise, topography-independent placement of uncontaminated, reproducible and well-defined plasmonic nanostructures, including optical antennae. We demonstrated the utility of IDML by fabricating and characterizing Au bowtie optical antennae on flat substrates. We then showed the flexibility of this novel technique by fabricating an optically functional antenna on an AFM tip apex with ∼5 nm position resolution and obtaining significant Raman enhancement.

2. Novel nanofabrication of optical antennae

Figure 1 depicts the induced-deposition mask lithography (IDML) process, which consists of three steps: (1) deposition of the desired antenna material, (2) precise placement of the etch mask via FEBID and (3) Ar ion milling, exploiting the energy-dependent relative etch rates for the antenna and mask materials, to transfer the mask into the material of interest. Si contact mode cantilevers (Nano World Cont 0.2 N m^{-1}) were prepared for IDML antennae fabrication by cutting off the apex of an AFM tip using FIB to form a mesa of ∼300 nm diameter parallel to the eventual sample surface. The IDML method can be used to fabricate a wide range of nanostructures of various materials, including single crystals, on many types of substrates while avoiding contamination during the fabrication process. It can achieve feature resolution below 10 nm, comparable with state-of-the-art EBL. Here, we fabricate bowtie-like optical antennae, formed by two opposing metallic nanotriangles, with a reproducible 12 nm gap.

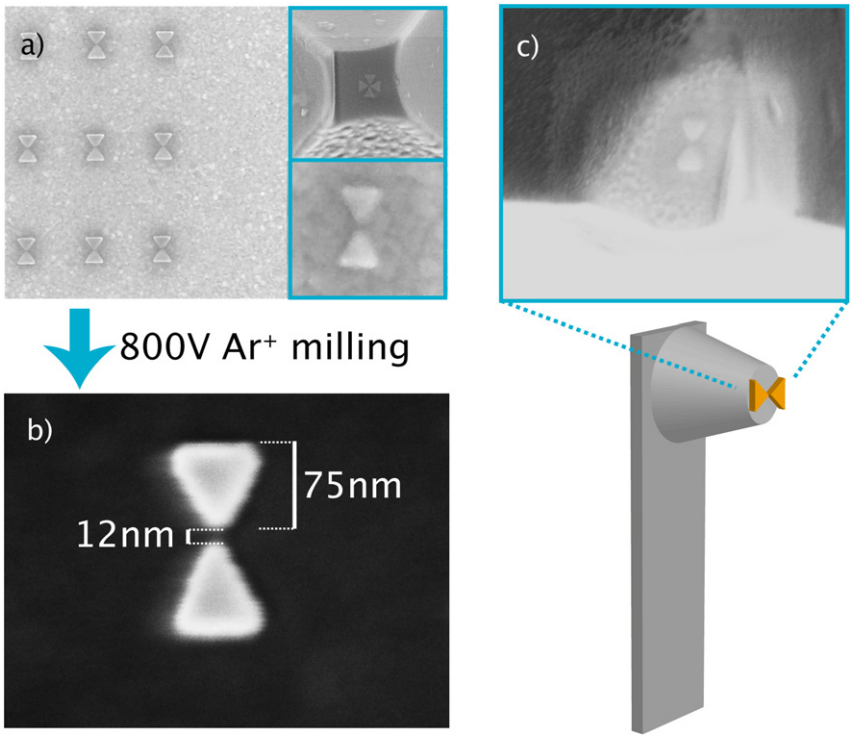

Figure 2. IDML method applied to form bowtie antennae. (a) SEM image of an array of FEBID SiO_x masks on Au. The top inset is a double-bowtie 'cross' W mask on an AFM tip mesa and the lower inset is a close-up of an SiO_x mask. (b) Au optical bowtie antenna after Ar^+ milling. (c) Au bowtie on an Si AFM tip.

A modified Zeiss XB1540ES crossbeam was used for IDML fabrication. This instrument was equipped with a commercial Zeiss gas injection system, a Xenos pattern generator that steered either the electron beam or the ion beam, and a NTI argon ion gun for *in situ* Ar^+ milling.

W and SiO_x mask materials were used for this work, and their respective precursors are tungsten hexacarbonyl and tetraethyl-ortho-silicate. W and SiO_x each exhibit a higher-energy sputter threshold for argon than Au [27], enabling efficient mask transfer. The use of W gave the best mask resolution, but during the subsequent milling process W flakes pealed off and surrounded the mask, decreasing the reproducibility of the Ar^+ etching process. In addition, W residues remaining on the antenna surface can shift the plasmon resonance or short-out the antenna. With SiO_x the mask resolution was slightly reduced but the subsequent milling process was more reliable.

For this work, 20 nm thick Au films with a 1 nm Cr adhesion layer were deposited on commercial Si wafers via sputter-coating since this method produced the smoothest films (see also supplementary information available at stacks.iop.org/Nano/21/065306/mmedia), silicon oxide cover slips or AFM tips (Si point tip Nano World Cont 0.2 N m^{-1}). The masks were subsequently defined via high-resolution FEBID. The precursors were introduced via gas injection needles in close proximity to the substrate [24]. While the gas valve was opened during exposure the pressure in the chamber increased 2×10^{-6} mbar. The resolution in FEBID is very sensitive to the accelerating voltage, beam current and density of precursor gas on the material [24, 28]. We found that 20 kV primary electron energy gave the best compromise between mask resolution and mask deposition rate for both W and SiO_x [29] precursors. Therefore, we systematically investigated the deposition parameter space (exposure dose, e-beam dwell time, etc) to achieve the highest mask resolution (see the supplementary information available at stacks.iop.org/Nano/21/065306/mmedia for details). Examples of bowtie masks are shown in figure 2(a). The antenna triangles were 75 nm long with a tip radius between 2 and 3 nm and a gap of 10 nm.

The transfer of the mask into the equivalent Au structure was achieved with Ar^+ milling, exploiting the differential etch characteristics between the mask and the Au film. In the time required for mask removal, the surrounding Au film and Cr adhesion layer were completely sputtered away, translating the mask shape with high accuracy into the underlying Au (figure 2(b)). The sample was sputtered 10° off the surface normal to obtain relatively vertical sidewalls. The Ar^+ energy used was 0.8 keV, the Ar^+ current 10 μA and the sputter spot size was 1 mm^2. The etch time was typically between 180 and 200 s, and depended on the Au film thickness and quality. For every new Au evaporated layer we made sputtering tests before etching the actual device. To ensure an Au- and Cr-free gap—essential for the functionality of the bowtie antenna—the samples were etched 20% longer than the time necessary to remove the Au and Cr layer. Therefore, the Au and Cr were also sputtered off the AFM tip sidewalls, where the Au thickness is less but the sputtering rate is reduced due to the flat incident angle. The only Au residues observed via SEM on

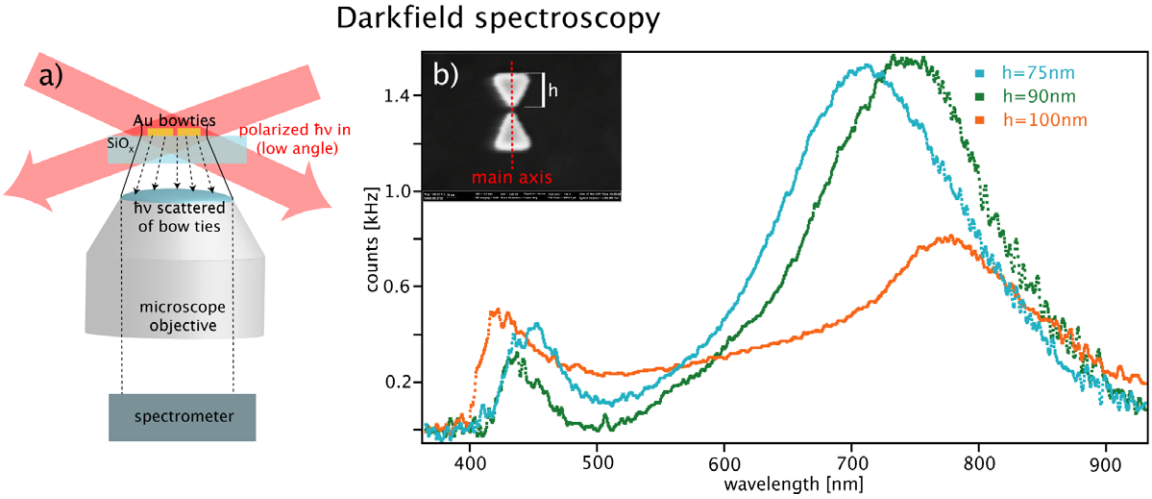

Figure 3. Resonance measurement of the fabricated optical antennae. (a) Diagram of the dark-field spectroscopy set-up used to determine the resonant frequency of the optical antennae. (b) Inset: bowtie with main axis and triangle length, h, marked. Main: dark-field spectra from three bowtie antennae. Increasing the length of the triangle redshifts the major peak position.

an AFM cantilever, other than the optical antenna, was in the kink between cantilever and the base of the tip pyramid, which does not compromise the actual functionality of the device.

Reproducible Au bowties composed of equilateral 75 nm long triangles with a 5 nm radius of triangle–tip curvature gap sizes of 12 nm were obtained (compare figure 2(b)). No impurities were detected by Auger spectroscopy in the resulting Au structures, once surface contamination was removed by mild Ar sputter cleaning. Figure 2(c) illustrates the ability of IDML to place well-defined reproducible antennae on an FIB-cut AFM tip mesa. The bowtie tip presented here was created using an SiO_x mask.

3. Determining the resonance frequency via dark-field spectroscopy

We use dark-field spectroscopy to measure the surface plasmon resonances of our *individual* metal nanoantennae [30] in a transmission confocal modality: white light is focused on the back of the transparent sample with a high numerical aperture (NA) oil condenser (NA = 1.43–1.2) and scattered light is collected with a 100×, 0.95 NA air objective, focused through a 150 μm diameter pinhole, then directed into a 0.3 m spectrometer (PI-Acton) and dispersed onto a liquid-nitrogen-cooled charge-coupled-device (CCD) camera. Figure 3(a) depicts our experimental set-up. In the case of asymmetric and/or coupled plasmonic devices, the resonance, scattering intensity and near-field enhancement depended on the polarization of the incoming light [18]. The scattered light of the bowties was collected by a microscope objective and coupled to a spectrometer with a charge-coupled-device (CCD) detector. The spectra were corrected for source intensity and spectrometer response variations.

Figure 3(b) shows the spectra of three different bowtie antennae. The single-triangle length (compare the inset in figure 3(b)) of the three sizes of bowties was 75, 90 and 100 nm, and the gap between the triangles was 12–14 nm. All three spectra contain two peaks, a minor peak at shorter wavelength and a major one at longer wavelength. We attribute the major peak to the dipolar plasmon resonance of a bowtie antenna [16, 18], which, for the 75 nm antenna (blue spectra), has a maximum at 710 nm. For the 90 nm bowtie (green spectrum), the major peak is redshifted to 760 nm due to the longer resonance cavity for the plasmon mode. The 100 nm bowtie is shifted further to 790 nm but shows a smaller scattering intensity, which we have to investigate further. The peak positions are consistent with bowties produced via e-beam lithography [18], effectively confirming the existence of a cavity for localized surface plasmons and validating the IDML nanofabrication method. The smaller peak is attributed to the quadrupole mode of the antennae and its spectral behavior is consistent with the calculations by Zhao *et al* [31].

It is important to note that the quality of the argon milling has a large impact on the resulting dark-field spectrum: over-sputtering the sample degrades the bowtie shape, leading to a featureless spectrum. On the other hand, if the Au and Cr adhesion layers are not completely milled through, then the triangles are not electrically isolated and form very lossy (and differently sized) optical cavities. This results in broad dark-field spectra with very few distinct features, as shown in figure S1 in the supporting information (available at stacks.iop.org/Nano/21/065306/mmedia), showing that dark-field spectroscopy is a sensitive measure of the fabrication quality. It was also possible to detect Cr via Auger spectroscopy in the vicinity of the bowtie after insufficient milling. However, by determining the proper etch rate we achieve a reproducibility of approximately 70% for this etching process determined via dark-field spectroscopy measurements over a variety of fabricated bowties (compare also figure S2 in the supporting information available at stacks.iop.org/Nano/21/065306/mmedia).

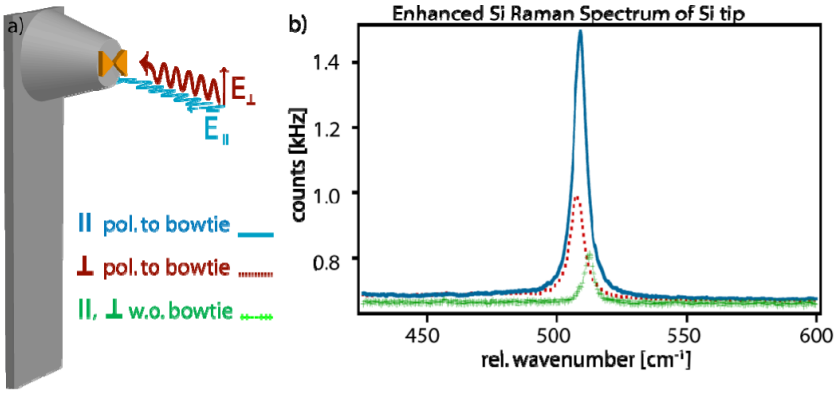

Figure 4. Raman signal enhancement due to a bowtie antenna on an Si AFM tip. (a) Diagram of the experimental Raman geometry. (b) The Raman spectra from Si AFM tips: when illumination is parallel (blue) to the bowtie's main axis, the total Si Raman line was 2.5-fold more intense than for perpendicularly polarized excitation (red). The green spectra was from an FIB-cut Si tip without an Au bowtie and showed no polarization dependence.

4. Near-field enhancement

We recorded Raman spectra of bowtie antennae fabricated on Si AFM tip mesas to evaluate the field enhancement, the crucial functional property of the antennae. Because silicon has a large Raman cross section, we observed an increase in the Si Raman signal when a functional bowtie was placed on the tip apex. Raman signals were recorded by mounting the bowtie AFM tips in a WITEC confocal Raman/AFM system. The tip was brought into contact with a clean silica cover slip. Polarized laser light was focused on the tip apex through the 300 μm thick cover slip using a 100×, 1.4 NA oil-immersion objective. The high Si dielectric function redshifts the resonance of the 75 nm bowties relative to those on flat silica, so we used a 785 nm diode laser to excite the bowties near their resonance. The polarization was tuned with a rotatable half-wave plate. No polarization-dependent power modulation was detected. The scattered light was collected by the same objective and passed through a beamsplitter and a 790 nm long pass filter into a spectrometer where the Si Raman line was measured. The focus was optimized by maximizing the Raman signal independently for each polarization: however, the maximum signal was obtained at the same focus for both cases.

First, the laser light was polarized along the bowtie's main axis (figure 4(a)) and a Raman spectrum was recorded, showing an Si Raman peak at 508 cm^{-1}. Subsequently, the polarization of the laser light was rotated 90° and a second Raman spectrum was recorded (figure 4(b)). A 2.5-fold stronger Raman signal was obtained with parallel polarization. The polarization dependence for each tip was repeated five times, reproducing the spectra shown here. In all, six tips were tested. For four of these, a polarization-dependent intensity increase between 1.7 and 2.5 was obtained. The other two tips showed no polarization-dependent effects. SEM examination showed that in one of these two cases, the triangles were connected, or 'shorted'. We suspect that this was true also for the second tip, but SEM examination was inconclusive. (High-resolution SEM observation renders bowtie tips inactive, likely due to carbon film deposition, which could short the nanoantenna.)

To ensure that the Raman polarization was not related to the Si crystal orientation, an identical FIB-flattened Si tip without a bowtie was placed into the NSOM. Figure 4(b) shows the resulting polarization-independent Si Raman spectrum in green. The lower peak intensity of the green spectrum compared to the blue and red spectra cannot be directly attributed to the absence of the bowtie since considerable tip-to-tip variations in absolute Si Raman intensity were observed. Interestingly, the peak position for the Si tip without bowties is shifted from 508 to 512 wavenumbers. Currently we do not understand the cause of the shift. A possible hypothesis is induced local strain in the Si due to the fabrication, which we will investigate.

Based on the observed intensity increase of 2.5 for the parallel versus perpendicular excitation polarization, it is possible to make an estimate of the near-field enhancement in the bowtie gap. There are two contributions to the Raman signal, one due to Raman scattering from the tip material in the (unenhanced) confocal volume and another due to the strongly enhanced field within the zeptoliter volume near the bowtie gap [7]. The ratio of these volumes times the polarization ratio gives an estimate of the enhancement in the bowtie gap. For the volume of the confocal spot V_c, we assumed a lateral Gaussian spot size with an FWHM of 280 nm based on the diffraction limit (λ = 785 nm, NA = 1.4) and a depth-of-focus of 820 nm, corresponding to the axial resolution of a confocal spot [32]. The volume contributing to the near-field-enhanced signal V_g is based on a conservative estimate of 20 nm gap size, resulting in a 400 nm^2 area times the 20 nm penetration depth of the evanescent wave into the silicon (details in supplementary information available at stacks.iop.org/Nano/21/065306/mmedia). The 2.5-fold signal intensity increase (150%) and the effective volume ratio leads to a Raman enhancement estimate of $1.5 \times V_c / V_g \approx 3.9 \times 10^4$. The total Raman enhancement is approximately proportional to the fourth power of the nanoantenna's electric field enhancement [33]. Therefore, the square root of the Raman enhancement gives an optical intensity enhancement of ~200 for the bowtie.

To our knowledge this is the first demonstration of Raman enhancement from a functional bowtie antenna placed on an AFM tip. This was enabled by the novel direct-write mask lithography fabrication method. This technique allows us to place nanostructures such as the Au bowtie with great flexibility and accuracy on insulating, semiconducting or conducting surfaces with various topographies, including on AFM tips. Hence, this novel fabrication technique can integrate genuinely functional nanostructures within larger scale devices and frameworks, i.e. it is ideal for the development of novel scanning probes, as shown here, or, more generally, for the implementation of specific nanostructures in complex assemblies. We demonstrated the capabilities of this technique by fabricating and characterizing optical antennae on scanning AFM probe tips, showing size-dependent resonance effects and optical intensity enhancement comparable with good EBL antennae. For future TERS measurements, the antennae will be fabricated on SiO_2 or SiN, since these will provide less Raman background.

Acknowledgments

The authors thank Ed Wong for fast and high quality technical support. This work was performed at the Molecular Foundry, Lawrence Berkeley National Laboratory, and was supported by the Office of Science, Office of Basic Energy Sciences, of the US Department of Energy under contract no. DE-AC02-05CH11231. M Schmidt is supported by the Energy Biosciences Institute.

References

[1] Soljacic M and Joannopoulos J D 2004 Enhancement of nonlinear effects using photonic crystals *Nat. Mater.* **3** 211–9
[2] Wurtz G A, Pollard R and Zayats A V 2006 Optical bistability in nonlinear surface-plasmon polaritonic crystals *Phys. Rev. Lett.* **97** 057402
[3] Mocella V *et al* 2009 Self-collimation of light over millimeter-scale distance in a quasi-zero-average-index metamaterial *Phys. Rev. Lett.* **102** 133902
[4] Valentine J *et al* 2008 Three-dimensional optical metamaterial with a negative refractive index *Nature* **455** 376-U32
[5] Bozhevolnyi S I *et al* 2006 Channel plasmon subwavelength waveguide components including interferometers and ring resonators *Nature* **440** 508–11
[6] Muhlschlegel P *et al* 2005 Resonant optical antennas *Science* **308** 1607–9
[7] Schuck P J *et al* 2005 Improving the mismatch between light and nanoscale objects with gold bowtie nanoantennas *Phys. Rev. Lett.* **94** 017402
[8] Stockle R M *et al* 2000 Nanoscale chemical analysis by tip-enhanced Raman spectroscopy *Chem. Phys. Lett.* **318** 131–6
[9] Hoppener C and Novotny L 2008 Antenna-based optical imaging of single Ca^{2+} transmembrane proteins in liquids *Nano Lett.* **8** 642–6
[10] Hartschuh A 2008 Tip-enhanced near-field optical microscopy *Angew. Chem. Int. Edn* **47** 8178–91
[11] Hartschuh A *et al* 2003 Simultaneous fluorescence and Raman scattering from single carbon nanotubes *Science* **301** 1354–6
[12] Pettinger B *et al* 2004 Nanoscale probing of adsorbed species by tip-enhanced Raman spectroscopy *Phys. Rev. Lett.* **92** 096101
[13] Kuwata H *et al* 2003 Resonant light scattering from metal nanoparticles: practical analysis beyond Rayleigh approximation *Appl. Phys. Lett.* **83** 4625–7
[14] Barnes W L, Dereux A and Ebbesen T W 2003 Surface plasmon subwavelength optics *Nature* **424** 824–30
[15] Sundaramurthy A *et al* 2006 Toward nanometer-scale optical photolithography: utilizing the near-field of bowtie optical nanoantennas. *Nano Lett.* **6** 355–60
[16] Merlein J *et al* 2008 Nanomechanical control of an optical antenna *Nat. Photon.* **2** 230–3
[17] Compton R C *et al* 1987 Bow-tie antennas on a dielectric half-space—theory and experiment *IEEE Trans. Antennas Propag.* **35** 622–31
[18] Fromm D P *et al* 2004 Gap-dependent optical coupling of single 'Bowtie' nanoantennas resonant in the visible *Nano Lett.* **4** 957–61
[19] Sun Y G and Xia Y N 2002 Shape-controlled synthesis of gold and silver nanoparticles *Science* **298** 2176–9
[20] Nobile C *et al* 2008 Probe tips functionalized with colloidal nanocrystal tetrapods for high-resolution atomic force microscopy imaging *Small* **4** 2123–6
[21] Taminiau T H *et al* 2007 lambda/4 resonance of an optical monopole antenna probed by single molecule fluorescence *Nano Lett.* **7** 28–33
[22] Cubukcu E *et al* 2006 Plasmonic laser antenna *Appl. Phys. Lett.* **89** 093120
[23] Malinsky M D *et al* 2001 Chain length dependence and sensing capabilities of the localized surface plasmon resonance of silver nanoparticles chemically modified with alkanethiol self-assembled monolayers *J. Am. Chem. Soc.* **123** 1471–82
[24] Utke I, Hoffmann P and Melngailis J 2008 Gas-assisted focused electron beam and ion beam processing and fabrication *J. Vac. Sci. Technol.* B **26** 1197–276
[25] Mitsuishi K *et al* 2003 Electron-beam-induced deposition using a subnanometer-sized probe of high-energy electrons *Appl. Phys. Lett.* **83** 2064–6
[26] Utke I *et al* 2000 Focused electron beam induced deposition of gold *J. Vac. Sci. Technol.* B **18** 3168–71
[27] Yoshitake M, Yamauchi Y and Bose C 2004 Sputtering rate measurements of some transition metal silicides and comparison with those of the elements *Surf. Interface Anal.* **36** 801–4
[28] Guan Y F *et al* 2008 Nanoscale lithography via electron beam induced deposition *Nanotechnology* **19** 505302
[29] Wanzenboeck H D *et al* 2006 Custom design of optical-grade thin films of silicon oxide by direct-write electron-beam-induced deposition *J. Vac. Sci. Technol.* B **24** 2755–60
[30] McFarland A D and Van Duyne R P 2003 Single silver nanoparticles as real-time optical sensors with zeptomole sensitivity *Nano Lett.* **3** 1057–62
[31] Zhao L L, Kelly K L and Schatz G C 2003 The extinction spectra of silver nanoparticle arrays: influence of array structure on plasmon resonance wavelength and width *J. Phys. Chem.* B **107** 7343–50
[32] Diaspro A 2002 *Confocal and Two-Photon Microscopy* ed A Diaspro (New York: Wiley) p 110
[33] Schatz G C and Van Duyne R P 2002 Electromagnetic mechanism of surface-enhanced Raman spectroscopy *Handbook of Vibrational Spectroscopy* ed J M Chalmers and P R Griffiths (Chichester: Wiley)